ACS OMEGA

http://pubs.acs.org/journal/acsodf

Article

Electroreduction of CO_2 and Quantification in New Transition-Metal-Based Deep Eutectic Solvents Using Single-Atom Ag Electrocatalyst

Ahmed Halilu,* Mohamed K. Hadj-Kali,* Mohd Ali Hashim, Emad M. Ali, and Suresh K. Bhargava

Cite This: *ACS Omega* 2022, 7, 14102−14112

Read Online

ACCESS | Metrics & More | Article Recommendations | Supporting Information

ABSTRACT: Deep eutectic solvents (DESs) are efficient media for CO_2 capture, and an electroreduction process using the deterministic surface of single-atom electrocatalysts is a facile way to screen gas absorption capacities of novel DESs. Using newly prepared transition-metal-based DESs indexed as TDESs, the interfacial mechanism, detection, quantification, and coordination modes of CO_2 were determined for the first time. The CO_2 has a minimum detection time of 300 s, whereas 500 s of continous ambient CO_2 saturation provided $ZnCl_2$/ethanolamine (EA) (1:4) and $CoCl_2$/EA (1:4) TDESs with a maximum CO_2 absorption capacity of 0.2259 and 0.1440 mmol/L, respectively. The results indicated that CO_2 coordination modes of η^1 (C) and η^2 (O, O) with Zn in $ZnCl_2$/EA (1:4) TDESs are conceivable. We found that the transition metals in TDESs form an interface at the compact layer of the electrocatalyst, while $CO_2^{\bullet-}$/CO_2 reside in the diffuse layer. These findings are important because they provide reliable inferences about interfacial phenomena for facile screening of CO_2 capture capacity of DESs or other green solvents.

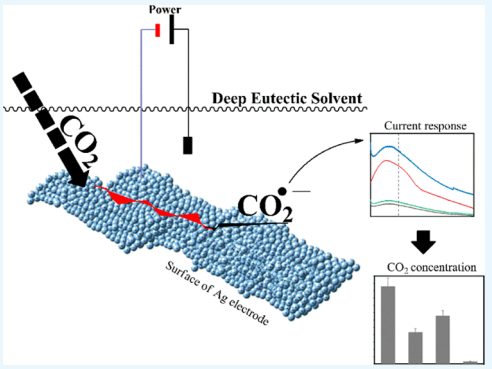

1.0. INTRODUCTION

Global carbon dioxide (CO_2) concentrations have reached ~420 ppm,[1] the highest level since precise measurements began 63 years ago.[1,2] As evidence of the link between high CO_2 emissions and global warming grows, it becomes important to develop simple and sustainable CO_2 sequestration strategies.[3−8] The need for long-term CO_2 sequestration cannot be overstated because it can provide CO_2 as a cheap C-1 feedstock for the production of low molecular weight hydrocarbons,[9] platform chemicals,[10−14] sustainable energy through electroreduction,[15,16] and energy storage.[17,18] Therefore, the facile measurement of CO_2 concentration in green solvents is essential to support the mitigation of anthropogenic CO_2 emissions and industrial CO_2 utilization.

Deep eutectic solvents (DESs) have shown promise in dissolving larger amounts of CO_2 than the conventional solvents used for CO_2 sequestration.[19−26] DESs are prepared from a suitable ratio of at least one hydrogen bond donor (HBD) and one hydrogen bond acceptor (HBA) component without generating byproducts that would require additional purification.[27] Although conventional DESs are prepared and used for high-pressure CO_2 sequestration, CO_2 electroreduction in DESs is a promising strategy to assess CO_2 from a point source. Several properties common to DESs (e.g., low current density, high viscosity, and high water) are known to contribute to side reactions, such as hydrogen evolution, during the CO_2 electroreduction. These are the challenges that likely hinder a scalable development of an effective DES medium for CO_2 sequestration. Also, the low CO_2 absorption of some DESs and the puzzling coordination mechanism by which these DESs could facilitate CO_2 sequestration are still unclear. The low CO_2 sorption of some DESs necessitates the use of transition-metal-based DESs, as they have ambient CO_2 sorption capacity. However, these challenges compel the tuning of common DESs to exhibit multifunctional properties such as high gas absorption capacity, low degradation rate, easy regeneration, low toxicity, and high physicochemical stability for task-specific applications.[21,28] Since countless combinations of HBDs and HBAs are possible, there are numerous opportunities to develop novel DESs with effective CO_2 sequestration capacity.

The common DESs explored for CO_2 sequestration by volumetric or pressure-drop techniques that exhibited appreciable CO_2 solubility were prepared using choline (ChCl) precursors.[29,30] To illustrate, Leron et al.[31] found a CO_2 solubility of 2.5 mol/kg in (ChCl)−glycerol (1:2) at 25 °C and 6 MPa (59.22 atm). Others observed a CO_2 solubility of 5.16 mol/kg in ChCl−urea (1:2) (123.37 atm) at 40 °C and 12.5 MPa.[32] The relative CO_2 capture performance of ChCl-based DESs was due to additive CO_2 sorption via weak van der

Received: February 2, 2022
Accepted: March 30, 2022
Published: April 18, 2022

Waals forces between CO_2 and nitrogen, including the propensity of HBD to absorb CO_2.[33,34] These pneumatic measurements of CO_2 solubility in DESs are limited by buoyancy forces that restrict precise measurements of gas solubility, the inability to detect low gas concentrations, especially at low pressure, and the need for a large volume of solvent. Therefore, it is highly non-facile to screen different promising DESs for CO_2 sorption using only the pneumatic effects.

In this study, a simple electrochemical cell was built as an instrument to measure CO_2 solubility in DESs under ambient conditions. Another experimental setup was created to estimate the electrochemical double layer in the CO_2-saturated DESs. The setup includes a custom-made vacuum-capable three-electrode electrochemical cell with three electrodes inserted into a closed environment where saturation with inert gas can be ensured to eliminate moisture that could saturate DESs. The CO_2 gas line was equipped with a pressure gauge strategically placed outside the cell but routed through a gas line to the electrochemical cell. This device eliminates moisture by saturating the cell environment with ultrapure inert gas. Therefore, for the first time, the detection of CO_2 at an interface between a single-atom Ag electrocatalyst and various newly prepared transition-metal-based deep eutectic solvents indexed as TDESs was investigated. First, eight TDESs were synthesized from transition-metal-based HBAs and corresponding HBDs such as ethanolamine (EA) and ethylene glycol (EG). The glass transition temperature, thermal transition, and ionic conductivity properties of the TDESs were determined. The TDESs were designed and prepared based on their ability to form interactions with π-orbitals of CO_2 through the transition metal sites.[35−37] The interaction between CO_2 and different transition metal surfaces is already known.[38−41] Since TDESs have hydrophobic and hydrophilic sites, they are likely to attract water. To address this issue, they were thoroughly dried and stored in a saturated inert environment to eliminate any tendency toward moisture during the electroreduction process. The elimination of moisture is necessary to prevent any possible CO_2 and H_2O coelectrolysis or the hydrogen evolution reaction. Therefore, the electroreduction technique involves simultaneous CO_2 electroreduction, with limiting currents approaching a steady state or stationary current. Accordingly, CO_2 concentrations are determined from the current responses, while the electrochemical double-layer capacitance at the CO_2-TDESs/Ag electrode interface was estimated using potentiostatic electrochemical impedance spectroscopy (PEIS) for the first time. These analyses in conjunction with the frontier molecular orbital (FMO) for CO_2-TDESs provided insights into the interaction mechanisms of CO_2 with the transition metal sites in TDESs. Moreover, the COSMO-RS analysis was used to understand the CO_2 absorption capacity of the $-NH_2$ and $-OH$ functional groups on the TDESs. The study combined a portfolio of analyses to provide inferential information about interfacial CO_2 circumstances and a facile electrochemical approach of screening the gas absorption capacity of green solvents. It also elucidates CO_2 coordination modes and provides insights into CO_2 electrocatalysis driven by a single-atom electrocatalyst.

2.0. MATERIALS AND METHODS

2.1. Materials. Table 1 shows the chemicals used in this study together with their purities and sources. The chemical precursors were used without further purification. The fixtures such as electrodes for the CO_2 solubility measurement include: Pt wire (5.7 cm, BASi Inc.) as a counter electrode, silver (Ag) (OD: 6 mm, ID: 3 mm) electrode as a working electrode, and Ag/AgCl (6 mm) as a reference electrode.

Table 1. Description of the Materials Used in This Study

chemicals	purity (% mass)	company/source
CO_2	99.999	Gas link SDN, Malaysia
N_2	99.999	Gas link SDN, Malaysia
zinc chloride ($ZnCl_2$)	>99	Chemiz, Malaysia
nickel II chloride hexahydrate ($NiCl_2{\cdot}6H_2O$)	>98	Merck, Darmstadt, Germany
cobalt II chloride hexahydrate ($CoCl_2{\cdot}6H_2O$)	>98	ACROS Organics, New Jersey, USA
copper II chloride dihydrate ($CuCl_2{\cdot}2H_2O$)	>98	R&M chemicals, Essex, U.K.
ethylene glycol	>99	Darmstadt, Germany
ethanolamine	>99	Sigma-Aldrich, Darmstadt, Germany

2.2. Preparation of TDESs. The TDESs were prepared by constant mixing of HBA ($ZnCl_2$, $NiCl_2{\cdot}6H_2O$, $CuCl_2{\cdot}2H_2O$, and $CoCl_2{\cdot}6H_2O$) and HBD (ethanolamine and ethylene glycol) components in a molar ratio of 1:4 at 70 °C for 8 h, similar to the DES synthesis procedure reported by Abbott et al.[27] This temperature level was verified as not sufficient to trigger any chemical reaction between the HBA and HBD but to promote solubilization of HBA in HBD during the process of forming a eutectic mixture. In addition, the indexed TDESs were confirmed to be eutectic mixtures and not a normal mixture of the HBD and HBA precursors. After synthesis, the TDESs were subjected to a one-month aging process, and they maintained their fluidity without any recrystallization.

2.3. Thermal Gravimetric Analysis (TGA). Experiments were carried out using a PerkinElmer model TGA-7 thermogravimetry system to determine the degradation temperature of the TDESs (T_d). The system contains a microprocessor driven by a temperature control unit and a data acquisition station. The tests were carried out in a nitrogen atmosphere, with TDES samples weighing 5−6 mg packed in aluminum pans. The TDES mass in the sample pan was continuously recorded as a function of temperature to account for any possible degradation. The TDES samples were heated from 27 to 700 °C at a constant rate of 10 °C/min. The presented TGA results are the mean of at least two measurements.

2.4. Differential Scanning Calorimetry Analysis (DSC). Calorimetric experiments were carried out with a PerkinElmer DSC-8000 operating in the heat flow option to evaluate the thermal behavior of the TDES samples. The measurements were carried out in dry high-purity nitrogen at a flow rate of 20 mL/min. In T_{zero} aluminum pans, less than 5 mg of each sample was encapsulated. The set was not hermetically sealed, allowing for free evaporation of water. At least two scans were performed at cooling and heating rates of 10 °C min^{-1}, covering the temperature range of −70 to 100 °C. At the end of the scan, each sample was kept at 100 °C for an additional minute to ensure water removal. In addition, each sample was kept at −70 °C for 10 min to obtain a better signal of the glass transition temperature, if present.

2.5. Ionic and Flow Properties of TDESs. Initially, the water content of the TDESs was determined after drying under

https://doi.org/10.1021/acsomega.2c00672
ACS Omega 2022, 7, 14102−14112

a vacuum for 6 h at 55 °C upon preparation. Therefore, an 831 Karl Fischer Coulometer including a titration cell with a generator electrode without a diaphragm was used for H_2O content determination down to trace levels. Since the technique for detecting gas solubility requires electricity, we further determined and verified the conductivity of the TDESs. Accordingly, the conductivity of differently dried TDESs was measured using a multiparameter analyzer (CHEETAH model DZ2-708). The pH of the dried TDESs was also measured with a Benchtop pH meter (BP3001).

2.6. *In Situ* CO_2 Concentration at the TDESs/Ag Interface. The CO_2 concentration absorbed by the TDESs was determined using the chronoamperometry technique. A 10 mL membraneless electrochemical cell (Figure 1a) at 1 atm

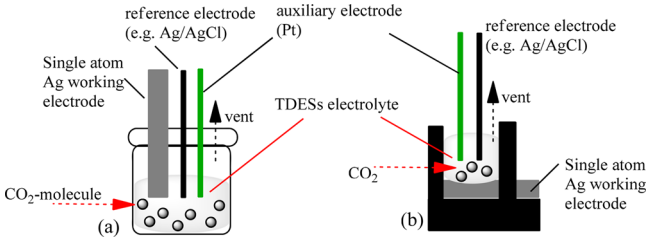

Figure 1. Schematic of (a) voltammetry for detecting CO_2 solubilities in TDESs and (b) EIS measurement of the double-layer capacitance at the interface between a single-atom Ag-electrocatalyst surface and CO_2-saturated TDESs.

pressure, sealed with a polytetrafluoroethylene (PTFE) cap, tapped with a gas line, and a three-electrode system was typically built and used to determine CO_2 absorption by TDESs. TDESs ($ZnCl_2$/EA, $NiCl_2$/EA, $CuCl_2$/EA, $CoCl_2$/EA, $ZnCl_2$/EG, $NiCl_2$/EG, $CuCl_2$/EG, and $CoCl_2$/EG) were dried prior to the experiments. The electrochemical cell was eventually filled with 5 mL of the dried TDESs, a Pt wire (5.7 cm, BASi Inc.) counter electrode, a silver (Ag) (OD: 6 mm, ID: 3 mm) working electrode, and a saturated Ag/AgCl (6 mm) reference electrode clamped therein. The process data were collected using an Autolab Potentiostat model PGSTAT302N connected to the electrochemical cell. The cell was placed in a jacketed glovebox saturated with N_2 during the measurement process to ensure a sterile environment in which only CO_2 sparged into the cell containing TDESs. As a result, the electrochemical process in the cell was controlled using the Nova 2.1 data acquisition software. A fixed CO_2 flow rate of 1 SCFH (0.47 L/min) into the electrochemical cell was maintained for a maximum of 700 s to measure CO_2 solubility in the TDESs at 25 °C. The Cottrell-like chronoamperometry profile was obtained by using a −1.5 V vs Ag/AgCl potential slightly above the onset potential for CO_2 electroreduction. Furthermore, at the onset of limiting currents ($I_{lim} \sim I_o$) that are momentarily transport controlled to approach a stationary current value (I_∞) where the rates of CO_2 consumption through chemical absorption and dissolution are equal, the CO_2 was simultaneously reduced. The current response given by eq 1[42] can be used to express the change in CO_2 concentration in the TDESs before reaching this stationary state. The experimental data were used to calculate $I = I(t)$, as well as the values of I_∞, I_o, and A_1. As a result, the equivalent weight of CO_2 was used in conjunction with eq 2 to calculate CO_2 concentration (C_o) values in the TDESs. Futhermore, the equilibrium rate constant (K_{eq}) for a typical CO_2 absorption by TDESs was determined using eq 3.[43] This enables estimation of the CO_2 absorption enthalpy in the TDESs using the Van't Hoff eq 4.[44] This is the enthalpy change that occurs when CO_2 is dissolved in TDESs following the reaction scheme: TDES + $2CO_2 \leftrightharpoons$ TDES-$2CO_2$.

$$I = I_\infty + (I_o - I_\infty)\exp(-A_1 t) \quad (1)$$

$$C_o = I_o^2/[zFA_1 v(I_o - I_\infty)] \quad (2)$$

$$K_{eq} = [\text{capacity}/(2 - \text{capacity})\cdot PCO_2^2] \quad (3)$$

$$\ln(K_{eq}) = (-\Delta H_{abs}/R) \times (1/T) + C \quad (4)$$

where $PCO_2 = 1$ since all experiments were carried out at atmospheric conditions; capacity = CO_2 absorption capacity by TDESs (mol L^{-1}); K_{eq} = reaction equilibrium constant (mol L^{-1} atm^{-1}); I_∞ = Stationary state current (mA/cm^2); I_{lim} = limiting current (mA/cm^2); C = concentration (M) [equiv/cm^3]; z = equivalent weight (g/equiv); F = Faraday constant (96485.3 C mol^{-1}); and v = volume of electrolyte (mL).

2.7. Electrochemical Double-Layer Capacitance at the CO_2-TDES/Ag Interface. The electrochemical double-layer capacitance (ECDL) is significant to show the presence of CO_2 at the TDES/Ag electrode interface. This indirectly supports the chronoamperometry estimation of CO_2 concentration at 1.5 V vs Ag/AgCl. Accordingly, the ECDL was measured using electrochemical impedance spectroscopy (EIS) on a biologic potentiostat (Sp-300) connected to the cell shown in Figure 1b. Throughout the process, the 1 SCFH (0.47 L/min) CO_2 flow rate was maintained while fixing 1.5 V vs Ag/AgCl potential, 10 mV amplitude, and 50 kHz to 50 mHz maximum frequency. Fresh CO_2-saturated TDESs were used throughout the ECDL measurement in an enclosed aluminum-based Faraday cage. Before each experiment, the single-atom Ag working electrode was polished using an alumina solution (BASi) and sonicated in distilled water to wade off other electroactive contaminants. The EC-Lab 11.31 software was used to fit the data acquired from the EIS measurements.

2.8. COSMO-RS and Frontier Molecular Orbital Analysis of CO_2 Interaction with TDESs. The conductor-like screening model for the realistic solvents (COSMO-RS) method based on BP-TZVP-C30-1401-CTD parametrization in COSMOthermX19 software[45,46] was used to theoretically validate the CO_2 interaction with TDESs. The TDESs were represented in the COSMO-RS analysis through an electro-neutral approach to realistically represent the TDESs. The transition metal halides HBAs used in preparing the TDESs were represented in COSMO-RS without water of hydration as a cutout plane. Therefore, the TDES compositions were formulated, and the geometries of the cutout planes were built and optimized based on individual HBAs and HBDs using the Hartree−Fock level of theory and a def-SV(P) basis set. The geometry optimization was achieved using the graphical user interface of the Turbomole software package version 4.0.[47] This was followed by a single-point calculation for each TDES cutout plane to generate the .cosmo files using the density functional theory (DFT)/Beck−Perdew-86 functional[48] and zeta valence potential (def-TZVP) basis set.[49] Eventually, the .cosmo files of TDES were generated further through the solubility job function in COSMOTthermX19 to predict the CO_2 concentrations in TDESs.

https://doi.org/10.1021/acsomega.2c00672
ACS Omega 2022, 7, 14102−14112

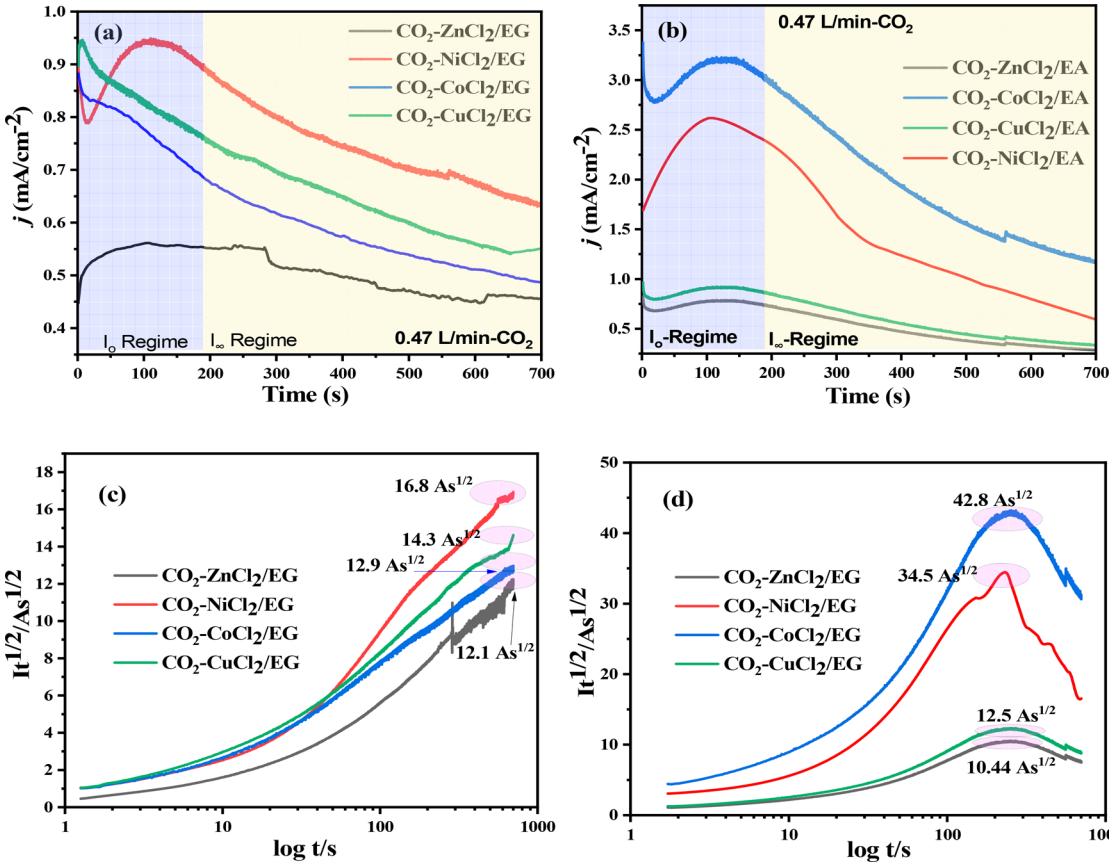

Figure 2. Dynamic current response of CO_2-saturated TDESs: (a) ethylene glycol TDESs, (b) ethanolamine TDESs, (c) Cottrell diffusion of CO_2 in ethylene glycol TDESs, and (d) Cottrell diffusion of CO_2 in ethanol amine TDESs. The dotted line in the Cottrel profile indicates the maximum value of the Cottrell parameter due to substantial ohmic and kinetic resistive contribution to the total current.

3.0. RESULTS AND DISCUSSION

3.1. Physicochemical Properties of TDESs. The TDESs were subjected to one month of aging, and they all retained their fluidity without recrystallization of the HBA precursors. The conductivity of the eight different TDESs at 298 K were shown in Table S1. In general, the EA-based TDESs exhibit higher conductivity than the EG-based DESs. These differences in conductivity are due to the fact that EA-based TDESs have much higher ion mobility than EG-based DESs. The ion mobility is due to the individual HBD or HBA sources. To demonstrate, the conductivity of the HBD sources such as EA is 48.2 μS/cm, which is higher than that of EG with 0.618 μS/cm. The conductivities of the ordinary transition-metal-based HBAs such as $ZnCl_2$, $NiCl_2{\cdot}6H_2O$, $CoCl_2{\cdot}6H_2O$, and $CuCl_2{\cdot}6H_2O$ are 36 200 μS/cm, 28 700 μS/cm, 32 100 μS/cm, and 13 710 μS/cm, respectively. Therefore, the conductivities of the formed TDESs are lower than those of the corresponding transition-metal-based HBAs. Since the conductivity of the EA-based TDESs is higher than that of the EG-based TDESs, the suppression of ion mobility by EA is much lower than that for EG. These observations confirm that HBDs suppress ion mobility when combined with transition-metal-based HBAs to form the TDESs. As shown in Table S1, the order of increase in conductivity for EA-based TDESs is $CuCl_2$/EA, $ZnCl_2$/EA, $NiCl_2$/EA, and $CoCl_2$/EA. Similarly, for EG-based TDESs, the order of conductivity increase is $CuCl_2$/EG, $ZnCl_2$/EG, $CoCl_2$/EG, and $NiCl_2$/EG. The ionic conductivity of $NiCl_2$/EA (20 400.2 μS/cm), $CoCl_2$/EA (26 400.2 μS/cm), $CoCl_2$/EG (12 610.2 μS/cm), and $NiCl_2$/EG (26600.2 μS/cm) is greater than that of allytriphenylphosphonium bromide/triethylene glycol (1:4, 670 μS/cm).[50] Although allytriphenylphosphonium bromide/triethylene glycol (1:4, 670 μS/cm) is not a TDES but it is in the sense of ordinary DESs, it consists of a 1:4 molar ratio of HBA/HBD which is the same ratio we used to prepare the TDESs shown in Table S1 (Supporting Information).

The thermal stability of TDESs was evaluated by TGA up to 550 °C, as shown in Figure S1. All the TDESs present a degradation peak above 120 °C decomposition temperature for coordinated water and another peak above 200−300 °C decomposition temperature for ligands. Dynamic TGA spectra usually show two basic onset decomposition temperatures (T_{onset}). The first decomposition temperature indicates surface water decomposition, while the second represents the decomposition of −OH, $-NH_2$, or chloride ligands. The T_{onset} is significant since it determines the maximum temperature at which DESs can retain their structure without breaking down.[51] Accordingly, Figure S1a and Figure S1b show the TGA spectra that distinguish the eight different TDESs based on whether they exhibit broad temperature to decomposition. As shown in Figure S1a−d, the values of T_{onset} for the TDESs are categorized as surface water or −OH or chloride ligands decomposition. The T_{onset} accrued for the loss of surface water in $ZnCl_2$/EG (1:4), $NiCl_2$/EG (1:4), $CoCl_2$/EG (1:4), and $CuCl_2$/EG is 53.4, 37.3, 48.0, and 61.3 °C, respectively. Similarly, the T_{onset} accrued for the decomposition of −OH or chloride ligands in $ZnCl_2$/EG (1:4), $NiCl_2$/EG (1:4), $CoCl_2$/EG (1:4), and $CuCl_2$/EG is 405.6, 460.5, 383.4, and 476.6 °C,

https://doi.org/10.1021/acsomega.2c00672
ACS Omega 2022, 7, 14102−14112

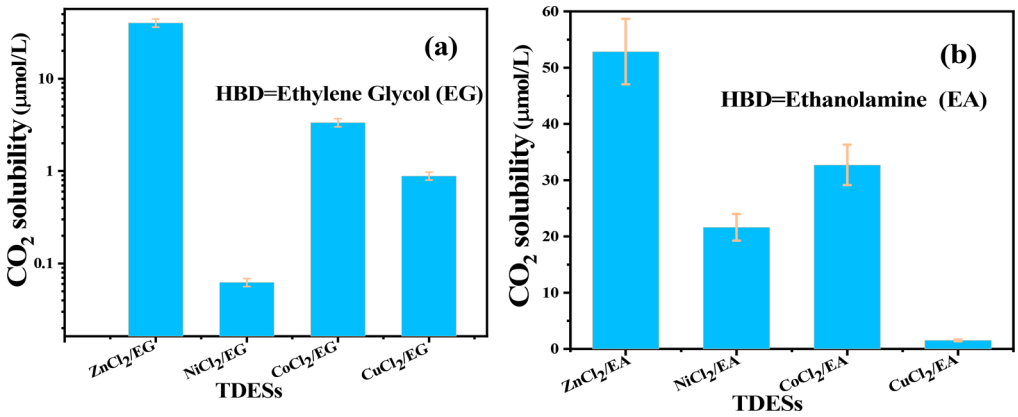

Figure 3. Screening effect of a hydrogen bond donor on the CO_2 absorption capacity of TDESs. (a) Ethylene glycol as HBD and (b) ethanolamine as HBD.

respectively. There is a small exception for EA-based TDESs with T_{onset} for the decomposition of surface water, −OH, $-NH_2$, or chloride ligands. Hence, Figure S1e−h shows the values of the T_{onset} for the EA-based TDESs. The T_{onset} accrued for loss of surface water in $ZnCl_2$/EA (1:4), $NiCl_2$/EA (1:4), $CoCl_2$/EA (1:4), and $CuCl_2$/EA is 58.5, 58.5, 45.2, and 50.6 °C, respectively. Accordingly, the T_{onset} for the decomposition of the −OH group in $ZnCl_2$/EA (1:4), $NiCl_2$/EA (1:4), CoCl/EA (1:4), and $CuCl_2$/EA is 189, 231.6, 242.4, and 218 °C, respectively. The T_{onset} for the decomposition of the $-NH_2$ group in $ZnCl_2$/EA (1:4), $NiCl_2$/EA (1:4), $CoCl_2$/EA (1:4), and $CuCl_2$/EA is 300, 300.9, 311.4, and 340.7 °C, respectively. The decomposition of the chloride ligands from the HBA site in $ZnCl_2$/EA (1:4), $NiCl_2$/EA (1:4), $CoCl_2$/EA (1:4), and $CuCl_2$/EA is 463.1, 535.1, 500, and 519.2 °C, respectively. These TGA results are significant and indicate that the TDESs can be dried at an average temperature of 52 °C. In general, $ZnCl_2$/EG (1:4), $NiCl_2$/EG (1:4), $CoCl_2$/EG (1:4), and $CuCl_2$/EG show two decomposition steps. Besides, $ZnCl_2$/EA (1:4), $NiCl_2$/EA (1:4), $CoCl_2{\cdot}6H_2O$/EA (1:4), and $CuCl_2$/EA show three steps of decomposition. However, the overall depiction of decomposition in the TDESs comprised of −OH, $-NH_2$, or chloride ligands commences at a minimum temperature of 200 °C. This implied the TDES usage is not suitable at or beyond this temperature range. The temperature is consistent with onset decomposition temperature for chloride ligands and hydroxyl, which is reported to occur at ∼200−600 °C depending on the metal complex.[52,53] In summary, the TDESs present at least two degradation peaks at temperatures above ca. 100 °C with the first peak representing the loss of water molecules.

In addition, Figure S2 shows the DSC spectrum of EA and EG-based TDESs, indicating their respective crystallization temperature (T_c), glass transition temperature (T_g), and melting temperature (T_m) in a temperature range from 75 to 350 °C. In Figure S2a, the EA-based TDESs have $T_c \approx 70$ °C, $T_g \approx 60$ °C, and $T_m \approx 200-250$ °C. The values of T_c and T_g are close, while their T_m falls at a higher temperature range. There are no apparent temperature effects at 25 °C. Contrarily in Figure S2b, the EG-based TDESs have $T_c \approx 68$ °C, $T_g \approx 52$ °C for $NiCl_2$EG (1:4), $T_g \approx 60$ °C for $CoCl_2$/EG (1:4), and $T_m \approx 200-250$ °C. The detection of a glass transition from which a T_g value can be determined allows us to classify all the TDESs tested as glass formers. It corresponds to a change in the structure of the material from a glassy state to a rubbery state, or vice versa, which is reflected in a jump in the heat capacity.

3.2. Transient Current in CO_2-Saturated TDESs. The current responses of CO_2 electroreduction in TDESs prepared with EG and EA HBD are shown in Figure 2a. The current response profiles show two striking patterns in which there is a current plateau (I_o) that subsequently decreased with time and forming an asymptotic limits. This type of pattern is attributed to the Cottrell-like profile, especially for a typical redox process such as the electroreduction of CO_2. The −1.5 V vs Ag/AgCl potential assumed for $CO_2^{\bullet-}$ free radical formation was maintained during the process, similar to previous reports. For instance, the reports do not use deep eutectic solvents (DESs) but instead DES analogues such as 50 mol % of [Emim][TFO]/10 mM $KHCO_3/H_2O$,[54] 0.1 M n-Bu_4NPF_6/2.0 mM $[C_{10}mim][BF_4]$ + 1.0% H_2O/acetonitrile,[55] and 8 mM [POHmim]BF_4/acetonitrile.[53] Accordingly, the corresponding potentials recorded for CO_2 electroreduction in these media in chronological order are (−1.8 V vs Ag/AgCl), (−2.3 V vs Fc+/Fc), and (−2.5 V vs Fc+/Fc), respectively. Therefore, at −1.5 V vs Ag/AgCl potential, the current responses depend on the CO_2 diffusion rate to the surface of a single-atom Ag electrode. In the practical sense of gas diffusion, the TDESs increase the CO_2 coverage around the single-atom Ag electrode through absorption. This means that the current response is diffusion-driven due to the formation of the $CO_2^{\bullet-}$ free radical and will be highest in the instantaneous period of the process. These instantaneous periods, when CO_2 consumption and conversion to $CO_2^{\bullet-}$ by chemical absorption and dissolution are not equal, are represented by the I_o regime in Figure 2a and 2b. The current in the I_o regime is the onset of limiting currents ($I_{lim} \equiv I_o$) and approaches a stationary current value in the I_∞ regime. At the I_∞ regime, the rates of CO_2 consumption and conversion to $CO_2^{\bullet-}$ by chemical absorption and dissolution are equal. In particular, the limiting currents ($I_{lim} \equiv I_o$) for EG-based TDESs (Figure 2a) are lower than those for EA-based TDESs (Figure 2b). Considering that diffusion of CO_2 is usually the limiting step of the CO_2 electroreduction, the product $I(t)t^{1/2}$ yields a characteristic time-invariant but potential-dependent constant known as the Cottrell parameter.[42,56] The Cottrell parameter is shown in Figure 2c and 2d, as $I(t)t^{1/2}$ vs log t plots where the short-term behavior of the CO_2 electroreduction using the single-atom Ag electrode is characterized by a sharp maximum peak. Regardless of the TDES media, the Cottrell parameter shows

https://doi.org/10.1021/acsomega.2c00672
ACS Omega 2022, 7, 14102−14112

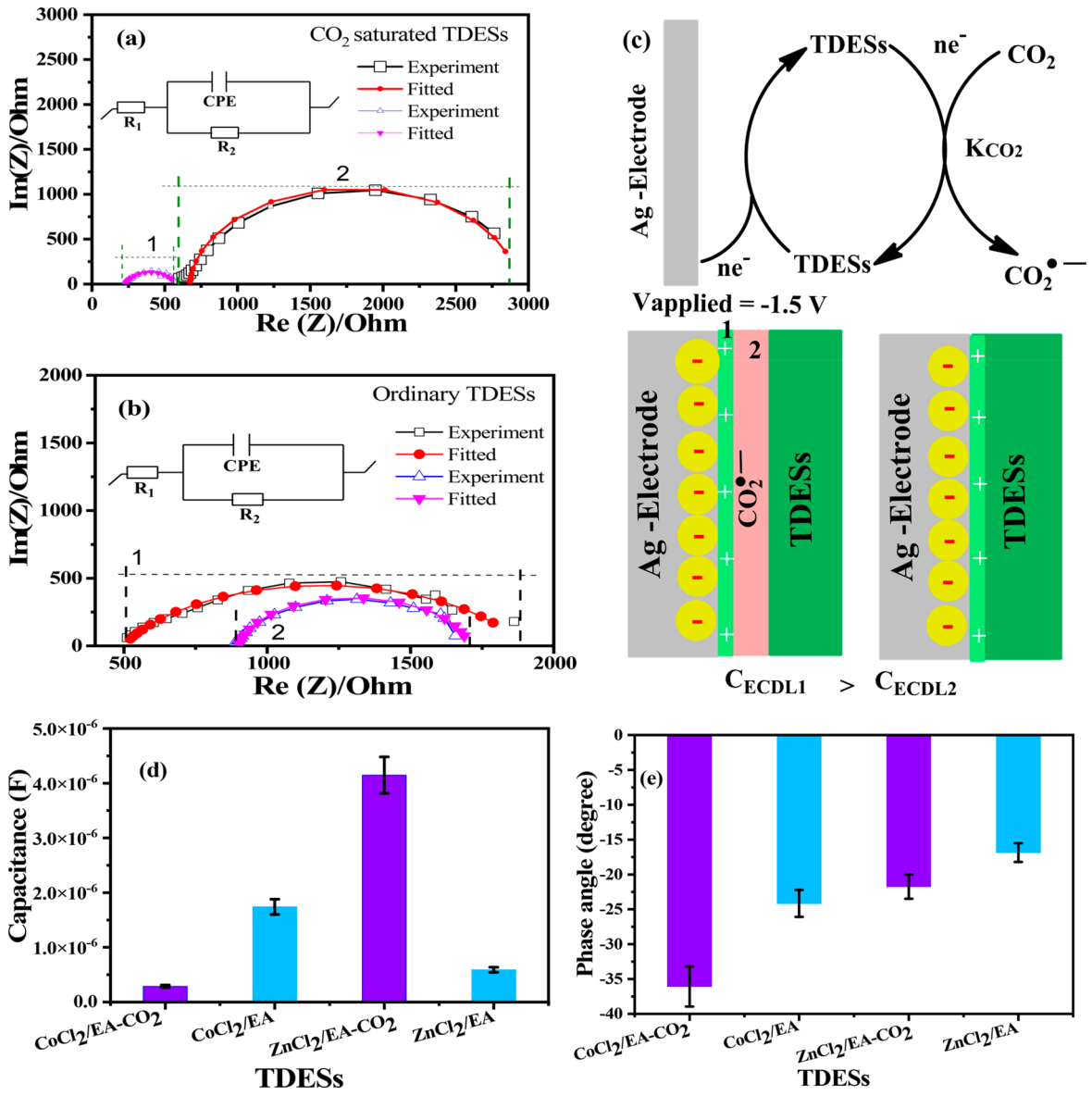

Figure 4. (a) Nyquist plot of CO_2-saturated TDESs: 1 = $ZnCl_2$/EA and 2 = $CoCl_2$/EA. (b) Nyquist plot of ordinary TDESs: 1 = $ZnCl_2$/EA and 2 = $CoCl_2$/EA. (c) Electrocatalysis depiction with an electron source. (d) Capacitance values of ordinary and CO_2-saturated $ZnCl_2$/EA and $CoCl_2$/EA. (e) Phase angle distortion values of ordinary and CO_2-saturated $ZnCl_2$/EA and $CoCl_2$/EA.

different maximum values. These values can be used to estimate $\tau_d = L^2/D$, which is the short term if substituted in $I(t) \equiv \Delta Q(\pi/\tau_d)^{-1/2}$, where $\Delta Q = \pm nF\Delta cAL$.

3.3. Measuring CO_2 Concentration in TDESs. *3.3.1. Effect of TDES HBDs on CO_2 Solubilities.* The CO_2 concentration in the TDESs was determined within the first 300 s of CO_2 flow to measure the influence of the two different HBDs, such as ethanolamine or ethylene glycol. In Figure 2, 300 s is a period characterized by unequal chemical absorption and dissolution. This means that CO_2 would always be present at the electrode surface for electroreduction at −1.5 V vs Ag/AgCl. Thus, the amount of CO_2 can be affected by the gas absorption tendency of TDESs with different HBD. Therefore, Figure 3a and Figure 3b shows the CO_2 concentration in TDESs with ethanolamine and ethylene glycol HBDs, respectively. The CO_2 concentration of ethanolamine-based TDESs is higher than that for ethylene glycol after 300 s of operation. The main reason for the low CO_2 concentration in ethylene glycol TDESs is the strong suppression of ion mobility by ethylene glycol. This leads to high ionic conductivity in ethanolamine (48.2 ± 0.2 μS/cm) and low ionic conductivity in ethylene glycol (0.618 ± 0.2 μS/cm). The low conductivity of ethylene glycol contributes to the overall low conductivity of the TDESs derived from it (see Table S1). Low conductivity imposes resistance to the electroreduction of CO_2 to generate an appropriate current response. Contrarily, the high CO_2 concentration in ethanolamine-based TDESs is due to four possibilities: $-NH_2$, −OH, transition metal surface, and high conductivity (see Table S1). However, ethylene-glycol-based TDESs have three possibilities such as −OH, transition metal surface, and low conductivity, so the CO_2 absorption capacity is lower here. The CO_2 concentrations in ethanolamine TDESs decrease in the following order: 5.304×10^{-5} mol/L ($ZnCl_2$/EA), 3.306×10^{-5} mol/L, ($CoCl_2$/EA), 2.180×10^{-5} mol/L ($NiCl_2$/EA), and 1.742×10^{-6} mol/L ($CuCl_2$/EA). Similarly, CO_2 concentration in ethylene-glycol-

https://doi.org/10.1021/acsomega.2c00672
ACS Omega 2022, 7, 14102−14112

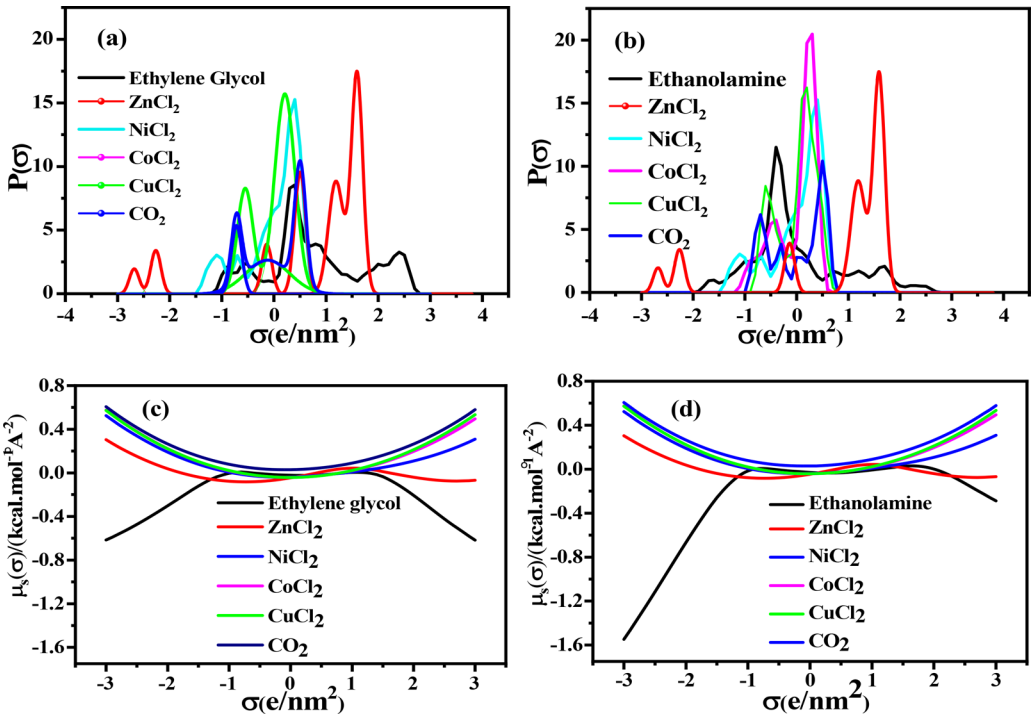

Figure 5. COSMO-RS analysis showing σ-profiles of (a) EG-based TDESs, (b) EA-based TDESs, and σ-potential of (c) EG-based TDESs and (d) EA-based TDESs.

based TDESs decreases in the following order: 4.015×10^{-5} mol/L ($ZnCl_2$/EG), 3.455×10^{-6} mol/L ($CoCl_2$/EA), 2.739×10^{-7} mol/L ($NiCl_2$/EA), and 1.253×10^{-6} mol/L ($CuCl_2$/EA). Although the CO_2 concentration in the ethylene-based TDESs is lower compared with ethanolamine, it is higher than that previously reported using pressure drop or electrochemical methods in a non-DESs medium. The comparison between the data from this present study with other studies in the literature is shown in Table S2. The table shows three possible categories of solvents and two main types of test methods. Our study highlights the first-time use of an electrochemical method to measure CO_2 concentration. This is an advance over the existing pressure drop or pneumatic method which requires high CO_2 pressure to increase its solubility. Table S2 compares the advances in different media and methods for CO_2 capture. It showed that the medium IL is suited for CO_2 capture but is limited by the high process conditions, especially when a nonelectrochemical method is used. Due to the exorbitant cost of ILs, the value for CO_2 capture cannot compensate for their cost. We envisage that DESs have the potential to complement existing media and that their further improvement is promising for high CO_2 sorption.

3.4. Electrochemical Double-Layer Capacitance at the CO_2-TDESs/Ag Interface. The electrochemical double-layer capacitance (ECDL) at the interface of CO_2-TDESs and the single-atom Ag was determined using potentiostatic-driven electrochemical impedance spectroscopy (EIS) as depicted in Figure 1a and Figure 1b. The EIS measurement was done at −1.5 V vs Ag/AgCl and a fixed CO_2 flow rate of 0.47 L/min into the $ZnCl_2$/EA and $CoCl_2$/EA TDESs. In this case, the CO_2-TDESs are CO_2-$ZnCl_2$/EA and CO_2-$CoCl_2$/EA. The CO_2 electroreduction is possible at −1.5 V vs Ag/AgCl, as indicated in Figure 1a and 1b. However, due to the low electrochemical potential window of TDESs which is typical of DESs, the double layer at the Ag electrode surface will contain ionic species such as $CO_2^{\bullet-}$ from CO_2, $C_3H_5O_4^-$ (zwitterions) from R-NH_2 functionality, or $-RCO_3^{2-}$ (carbonate ion) from R-OH functionality. This is particularly as the reduction window of the TDESs is less than 1.5 V vs Ag/AgCl. Moreover, by setting −1.5 V vs Ag/AgCl during the EIS measurement, the CO_2 undergoes electroreduction, while the TDES medium remains electrochemically likely to produce ions at the compact layer. We hypothesized that since the TDESs form the continuous phase they are localized, and the current response produced arises from the dispersed CO_2 electroreduction to the $CO_2^{\bullet-}$ free radical. The $CO_2^{\bullet-}$ free radical likely resides in the diffuse layer, i.e., the outer Helmholtz plane, while Co^{2+} or Zn^{2+} ionic species reside in the inner Helmholtz plane to facilitate electron transfer from the Ag electrode. These ionic species, depending on their spatial position on the electrode surface area, are capable of directly or indirectly forming an electrochemical double layer (EDL) that induces a distortion in phase angle. To validate the claim on phase angle distortion, we measured the impedance of the ordinary $ZnCl_2$/EA and $CoCl_2$/EA coupled with CO_2-$ZnCl_2$/EA and CO_2-$CoCl_2$/EA systems at −1.5 V vs Ag/AgCl. The Nyquist plot associated with the impedance measurement in the system before and after CO_2 absorption is shown in Figure 4a and 4b, respectively. The difference in Nyquist plot response before and after sparging CO_2 in $ZnCl_2$/EA and $CoCl_2$/EA indicates changes in the intermolecular interaction energy of the TDESs with CO_2, particularly at −1.5 V potentiostatic control. In Figure 4a, the Nyquist plot for the CO_2-$ZnCl_2$/EA system has a semicircle lower in diameter than the CO_2-$CoCl_2$/EA system. This result indicated faster charge transfer processes in CO_2-$ZnCl_2$/EA compared with CO_2-$CoCl_2$/EA. The semicircle is related to resistive-capacitive (RC) circuits.[54] Therefore, capacitance in association with the RC circuit of the Nyquist plot for the CO_2-$ZnCl_2$/EA or CO_2-$CoCl_2$/EA system was estimated by the equivalent circuit (EC)

https://doi.org/10.1021/acsomega.2c00672
ACS Omega 2022, 7, 14102−14112

shown in the inset of Figure 4a and 4b. The EC was fitted using two resistances, R_1 and R_2 coupled with a double-layer capacitance inform of the constant phase element (CPE). R_1 is the resistance of the TDESs media, while R_2 is the interfacial charge transfer resistance required for CO_2 electroreduction to the free radical. The pictorial depiction of the electrochemical transient states of CO_2, $CO_2^{\bullet-}$, and TDESs is shown in Figure 4c. Therefore, it was found that the capacitance of the $ZnCl_2$/EA medium according to Figure 4d is 0.59 μF before sparging CO_2. This is accompanied by the Faradaic charge transfer resistance of 348.6 Ohm (see Figure S3a). Moreover, after sparging CO_2, the capacitance of the $ZnCl_2$/EA medium increased to 4.149 F and was similarly accompanied by the Faradaic charge transfer resistance of 809.3 Ohm (see Figure S3a). Furthermore, the capacitance of the $CoCl_2$/EA medium is 0.287 F before sparging CO_2 and is accompanied by the Faradaic charge transfer resistance of 1418.1 Ohm (see Figure S3a). The capacitance of the $CoCl_2$/EA medium increased to 1.741 F when the medium was sparged and saturated with CO_2, the Faradaic charge transfer resistance is 2257.2 Ohm (see Figure S3a). The capacitance at the Ag electrode interphase does increase after sparging CO_2. This increase in interfacial capacitance upon CO_2 saturation in $CoCl_2$/EA or $ZnCl_2$/EA validates the intrinsic rationale behind the distortion in phase angle of CO_2-$CoCl_2$/EA or CO_2-$ZnCl_2$/EA media. For example, the phase angle detected in $ZnCl_2$/EA-CO_2 and $CoCl_2{\cdot}6H_2O$/EA-CO_2 after CO_2 saturation is higher than that detected in $ZnCl_2$/EA and $CoCl_2{\cdot}6H_2O$/EA before CO_2 saturation. In Figure 4e, the phase angles in CO_2-$ZnCl_2$/EA and CO_2-$CoCl_2$/EA are 36.08 and 21.75°, respectively. Moreover, the phase angles in $ZnCl_2$/EA and $CoCl_2$/EA are 24.16 and 16.86°, respectively. These results indicate that distortions in phase angle are possible due to CO_2 absorption by the TDESs and subsequent diffusion to the Ag-electrode surface, where it eventually undergo electroreduction to the $CO_2^{\bullet-}$ free radical. Our hypothesis for CO_2 behavior in TDESs using the single-atom Ag electrocatalyst is in congruence with the previous report that used nonresonant measurement of C−O adsorption on the Ag surface at 1.33 V vs Ag/AgCl.[57]

3.5. COSMO-RS Validation of the CO_2−TDES Interaction. COSMO-RS analysis was performed to validate linear CO_2 absorption by the TDESs which drag it near the surface of the single Ag-working electrode. It is only when linear CO_2 is substantially close to the surface of the single-atom Ag electrode that the $CO_2^{\bullet-}$ free radical will be generated. Therefore, the TDESs could assist in ensuring that the linear CO_2 coverage is high at the Ag surface through noncovalent interactions. The noncovalent interaction between linear CO_2 and the TDESs was estimated from their screening charge density and represented using σ-profiles. Accordingly, Figure 5a and 5b shows the σ-profile of linear CO_2 interaction with EG-TDESs and EA-TDESs, respectively. The σ-profile of linear CO_2 contains respite peaks at 0.7304 e/nm^2 or 0.5103 e/nm^2 screening charge density (see Figure 5a or 5b). These linear CO_2 screening charges fall within the nonpolar contribution area where σ-values are between −1.0 e/nm^2 and +1.0 e/nm^2.[58,59] As a result, we theorized that the screening charge densities on the symmetric electron function of linear CO_2 can signify the nonpolar contribution of the linear CO_2 interaction with TDESs. Usually, without sufficient energy supply, ordinary CO_2 is linear, and the COSMO-RS analysis is done to capture its interaction in this form, with the TDESs. Evidently, after energy is supplied to CO_2 it gains at least an electron to form a $CO_2^{\bullet-}$ free radical, and the geometry transforms from linear to bent over a likely angle of ∼150°.[60] The $CO_2^{\bullet-}$ free radical is not the form of energized CO_2 we are discussing here but rather neutral and non-energized CO_2. This is because the $CO_2^{\bullet-}$ free radical was generated after we have supplied −1.5 V vs Ag/AgCl. So, before supplying the −1.5 V vs Ag/AgCl, the TDES media were saturated with neutral CO_2 as illustrated by Figure 1a and 1b. We discovered that ethylene glycol (EG) HBD is characterized by typical noncovalent contributor screening charge densities of 0.480 e/nm^2 and 0.048 e/nm^2, respectively. Therefore, the neutral CO_2 with linear geometry can interact with the EG-HBD end in TDESs at their noncovalent contribution surfaces as shown in Figure 5a. Similarly, in Figure 5b, the neutral CO_2 can interact with ethanolamine (EA) at its noncovalent interaction site with screening charge densities of −0.388 e/nm^2.

The neutral CO_2 interact with noncovalent sites of $ZnCl_2$, $CoCl_2$, and $CuCl_2$ HBAs at −0.221, −0.401, or 0.269 and −0.625 or 0.204 e/nm^2 screening charge densities, respectively. These σ-profiles indicate the potential of neutral CO_2 interacting with the TDESs on the criterion of like dissolves like. In essence, the COSMO-RS analysis confirmed that similar nonpolar sites on the TDESs and CO_2 contributed to the physical CO_2 solubilization. Moreover, the various shapes of EA-HBD and EG-HBD σ-profiles provide further insight, indicating that CO_2 solubilization in these different TDESs is enthalpy driven. This means that the more soluble CO_2 is in TDESs, the less endothermic the enthalpy of solution will be, and vice versa. The σ-potential which is the plot of surface chemical potentials as a function of screening charge density was also determined for EG-based or EA-based TDESs, as shown in Figure 5c and Figure 5d. The highly negative σ-potential charge density greater than −0.955 e/nm^2 or 1.245 e/nm^2 is associated with negative polarity. This shows that EG or EA has an electron donor property, causing hydrogen to interact with the exposed oxygen atoms from the hydroxyl ends. For charge densities greater than 0.414 e/nm^2 or 0.302 e/nm^2, CO_2 has a positive σ-potential, showing that it has electron-accepting properties. Exceptionally, the $ZnCl_2$ HBA shows dual chemical potentials: (1) greater than 0.931 e/nm^2 which exhibits an electron-donating property and (2) greater than −2.019 e/nm^2, which possesses an rlectron-accepting tendency. Other HBA sites such as $NiCl_2$, $CoCl_2$, and $CuCl_2$ possess electron-donating tendency with negative chemical potential. These results are significant to confirm that neutral CO_2 absorbed through the HBA site in TDESs is more probable to generate the $CO_2^{\bullet-}$ free radical in a potential driven process. This is because in a potentiostatic process the inner Helmholtz layer is likely to be occupied by Ni^{2+}, Cu^{2+}, Co^{2+}, or Zn^{2+} species, and close to this layer, which is the outer Helmholtz layer, will be occupied by the $CO_2^{\bullet-}$ free radicals.

3.6. Interaction of CO_2 and Transition Metal Centers in TDESs. Figure 6 shows the interaction of CO_2 with the Zn surface in CO_2-$ZnCl_2$:EA based on frontier molecular orbital (FMO) analysis. Ordinary CO_2 gas and CO_2-$ZnCl_2$:EA were analyzed at DFT and semiempirical levels of theory, respectively. The results show that CO_2 interacts with the Zn transition metal based on the η^1(C) coordination mode (Figure 6a). The interacting inference can be deduced from the overlapping of the negative isosurface between 12Zn-5C. Typically, this form of interaction involves strong charge transfer between the d_z^2 transition metal orbitals and the

https://doi.org/10.1021/acsomega.2c00672
ACS Omega 2022, 7, 14102−14112

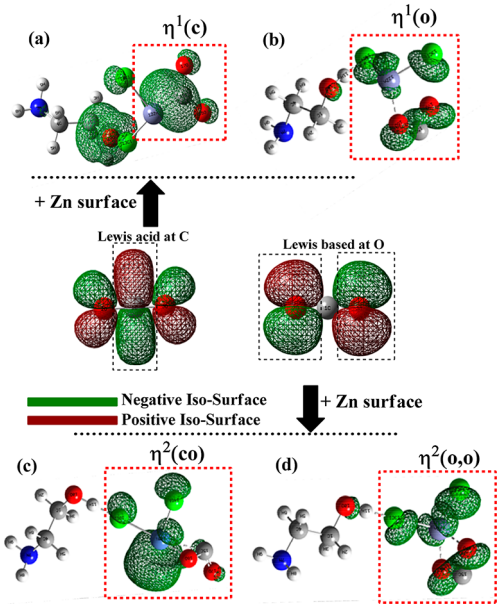

Figure 6. Mononuclear coordination of CO_2 to the transition metal surface. (a) η^1 CO_2 coordination modes, (b) η^1 (O)CO_2 coordination modes, (c) η^2 (O)CO_2 coordination modes, and (d) η^2 (O, O)CO_2 coordination modes. Calculation was done at the universal force field (UFF) level of theory.

antibonding π^* orbitals of CO_2.[61] Moreover, it is facilitated by an additional weak interaction between the two oxygen atoms of CO_2 and the Lewis acid center of the Zn metal's coordination sphere. Apart from the η^1(O) coordination mode, η^2(O,O) is also highly likely, as shown in Figure 6c, where the negative iso-surface around 12Zn-5C overlaps. The d-orbital sites in Zn accept electron pairs from carbonyl oxygen or π-orbitals as a case of typical Dewar−Chatt Duncanson interaction.[35−37,61,62] These interactions between CO_2 and TDESs are possible since as revealed from FMO analysis in Figure 6a−d, the carbon atom (LUMO orbitals) in CO_2 has a Lewis acid character typical of an electrophilic center, whereas the oxygens (HOMO orbitals) are weak Lewis bases representative of nucleophilic centers. Usually, the LUMO orbitals of CO_2 are occupied through the electron transfer from the Ag surface at −1.5 V to form the lowest energy state corresponding to a bent geometry. This implies that the linear form of CO_2 transforms to the $CO_2^{\bullet-}$ free radical with an equilibrium angle of 134°. The Zn surface was selected as a case study for illustration purpose. The same quantum chemical calculation can be applied to other transiton metal surfaces. Moreover, $ZnCl_2$/EA recorded high CO_2 concentration justifying its use as a case study herewith. Also, only two of the four [(η^1(C), η^2(C,O), η^1(O), and η^2(O,O)] possible CO_2 coordination modes were probable.

4.0. CONCLUSION

We employed theoretical and electrochemical experimental analysis to provide inferential insight into the detection and quantification of CO_2 in deep eutectic solvents for the first time. The study demonstrated electrochemical quantification of CO_2 solubilities in newly prepared transition-metal-based deep eutectic solvents indexed as TDESs for improved CO_2 sorption. The use of a transition metal precursor as a hydrogen bond acceptor to prepare the TDESs can induce additive sites for CO_2 sorption. Therefore, the structural factors such as incorporating a transition-metal-based HBA or HBD with an affinity for CO_2 and external factors such as the minimum gas saturation time are essential to ensure the TDESs' scalable applicability. Despite the number of studies on DESs and some conventional solvents, there is a scarcity of data for nonconventional solvents such as transition-metal-based DESs. Consequently, after screening different TDESs prepared using ethylene-glycol-based HBD for CO_2 capture capacity based on the chronoamperometry technique, this approach was successfully extended to different TDESs with ethanolamine-based HBD. The chronoamperometry technique used in screening the CO_2 capture has a facile detectable minimum time of 300 s. It was found that the coordination mode of CO_2 is dependent on the type of transition metal site in the TDESs. Moreover, the theoretical result confirmed that the CO_2-transition metal interaction can be visualized using negative iso-surfaces from the frontier molecular orbital analysis. Moreover, the CO_2 interacts with the proton in either NH_2 or OH via the involvement of positive iso-surface in their frontier molecular orbitals, typical of hydrogen bonding. Further investigation of double-layer capacitance indicated that a larger phase change of the CO_2-saturated medium seems most probable to confirm the free radical of CO_2 at the outer Helmholtz layer. On the contrary, the phase angle is low for the ordinary TDES medium without CO_2 saturation. The CO_2 being dispersed in the TDESs will always form ionic species in the outer Helmholtz layer, thereby increasing the capacitance and phase angle. This supports the hypothesis that Zn^{2+}, Ni^{2+}, Co^{2+}, and Cu^{2+} transition metal centers in TDESs reside at the inner Helmholtz layer. The results are significant in the facile screening of electrolytes or solvents for electrochemical CO_2 capture and utilization.

■ ASSOCIATED CONTENT

Supporting Information

The Supporting Information is available free of charge at https://pubs.acs.org/doi/10.1021/acsomega.2c00672.

Data on conductivity of TDESs and chemical precursors, thermal gravimetry analysis (TGA) and differential scanning calorimetry (DSC) of TDESs, dynamic CO_2 concentration, equilibrium constant of TDESs, and Faradaic information for TDESs such as capacitance, resistance, phase angle, and bode plot (PDF)

■ AUTHOR INFORMATION

Corresponding Authors

Ahmed Halilu − *Department of Chemical Engineering, Faculty of Engineering and University of Malaya Centre for Ionic Liquids (UMCiL), University of Malaya, Kuala Lumpur 50603, Malaysia;* orcid.org/0000-0003-0381-2365; Email: ahmed_h@um.edu.my

Mohamed K. Hadj-Kali − *Chemical Engineering Department, King Saud University, Riyadh 11421, Saudi Arabia;* orcid.org/0000-0002-1374-9825; Email: mhadjkali@ksu.edu.sa

Authors

Mohd Ali Hashim − *Department of Chemical Engineering, Faculty of Engineering and University of Malaya Centre for Ionic Liquids (UMCiL), University of Malaya, Kuala Lumpur 50603, Malaysia*

https://doi.org/10.1021/acsomega.2c00672
ACS Omega 2022, 7, 14102−14112

Emad M. Ali − *Chemical Engineering Department, King Saud University, Riyadh 11421, Saudi Arabia*
Suresh K. Bhargava − *Centre for Advanced Materials and Industrial Chemistry (CAMIC), School of Science, RMIT University, Melbourne 3001, Australia;* orcid.org/0000-0002-3127-8166

Complete contact information is available at: https://pubs.acs.org/10.1021/acsomega.2c00672

Notes

The authors declare no competing financial interest.

■ ACKNOWLEDGMENTS

Dr. Hadj-Kali would like to express his appreciation to the Researchers Supporting Project (RSP-2021/361), King Saud University, Riyadh, Saudi Arabia, for the financial support throughout this research.

■ REFERENCES

(1) NOAA. Carbon dioxide peaks near 420 parts per million at Mauna Loa observatory. https://research.noaa.gov/article/ArtMID/587/ArticleID/2764 (accessed 6th July, 2021).
(2) Hashimoto, K., Global temperature and atmospheric carbon dioxide concentration. In *Global Carbon Dioxide Recycling*; Springer: 2019; pp 5−17.
(3) Benson, S. M.; Orr, F. M. Carbon dioxide capture and storage. *MRS Bull.* **2008**, *33* (4), 303−305.
(4) Leung, D. Y.; Caramanna, G.; Maroto-Valer, M. M. An overview of current status of carbon dioxide capture and storage technologies. *Renew. Sustain. Energy Rev.* **2014**, *39*, 426−443.
(5) Meckling, J.; Biber, E. A policy roadmap for negative emissions using direct air capture. *Nat. Commun.* **2021**, *12* (1), 2051.
(6) Tollefson, J. Sucking carbon dioxide from air is cheaper than scientists thought. *Nature* **2018**, *558*, 173.
(7) UNFCCC, V. Adoption of the Paris agreement. https://unfccc.int/process-and-meetings/the-paris-agreement/the-paris-agreement (accessed 01/03/2022).
(8) Wilcox, J.; Haghpanah, R.; Rupp, E. C.; He, J.; Lee, K. Advancing adsorption and membrane separation processes for the gigaton carbon capture challenge. *Annu. Rev. Chem. Biomol. Eng.* **2014**, *5*, 479−505.
(9) Peterson, A. A.; Abild-Pedersen, F.; Studt, F.; Rossmeisl, J.; Nørskov, J. K. How copper catalyzes the electroreduction of carbon dioxide into hydrocarbon fuels. *Energy & Environ. Sci.* **2010**, *3* (9), 1311−1315.
(10) Kim, T.; Palmore, G. T. R. A scalable method for preparing Cu electrocatalysts that convert CO_2 into C^{2+} products. *Nature Commun.* **2020**, *11* (1), 3622.
(11) Fan, L.; Xia, C.; Zhu, P.; Lu, Y.; Wang, H. Electrochemical CO_2 reduction to high-concentration pure formic acid solutions in an all-solid-state reactor. *Nature Commun.* **2020**, *11* (1), 3633−3633.
(12) Halilu, A.; Hayyan, M.; Aroua, M. K.; Yusoff, R.; Hizaddin, H. F. In Situ Electrosynthesis of Peroxydicarbonate Anion in Ionic Liquid Media Using Carbon Dioxide/Superoxide System. *ACS Appl. Mater. & Interface* **2019**, *11* (29), 25928−25939.
(13) Halilu, A.; Hayyan, M.; Aroua, M. K.; Yusoff, R.; Hizaddin, H. F. Mechanistic insights into carbon dioxide utilization by superoxide ion generated electrochemically in ionic liquid electrolyte. *Phys. Chem. Chem. Phys.* **2021**, *23* (2), 1114−1126.
(14) Halilu, A.; Hayyan, M.; Aroua, M. K.; Yusoff, R.; Hizaddin, H. F.; Basirun, W. J. Hybridized Fe/Ru-SiMWCNT-ionic liquid nanofluid for CO_2 conversion into carbamate using superoxide ion. *J. Environ. Chem. Eng.* **2021**, *9* (4), 105285.
(15) Paz-Garcia, J. M.; Dykstra, J.; Biesheuvel, P.; Hamelers, H. Energy from CO_2 using capacitive electrodes−a model for energy extraction cycles. *J. Colloid Interface Sci.* **2015**, *442*, 103−109.
(16) Hamelers, H.; Schaetzle, O.; Paz-García, J.; Biesheuvel, P.; Buisman, C. Harvesting energy from CO_2 emissions. *Environ. Sci. & Techn. Lett.* **2014**, *1* (1), 31−35.
(17) Stevens, G. B.; Reda, T.; Raguse, B. Energy storage by the electrochemical reduction of CO_2 to CO at a porous Au film. *J. Electroanaly. Chem.* **2002**, *526* (1), 125−133.
(18) Wang, F.; Li, Y.; Xia, X.; Cai, W.; Chen, Q.; Chen, M. Metal−CO_2 Electrochemistry: From CO_2 Recycling to Energy Storage. *Adv. Energy Mater.* **2021**, *11* (25), 2100667.
(19) Zhang, N.; Huang, Z.; Zhang, H.; Ma, J.; Jiang, B.; Zhang, L. Highly efficient and reversible CO_2 capture by task-specific deep eutectic solvents. *Ind. Eng. Chem. Res.* **2019**, *58* (29), 13321−13329.
(20) Sze, L. L.; Pandey, S.; Ravula, S.; Pandey, S.; Zhao, H.; Baker, G. A.; Baker, S. N. Ternary deep eutectic solvents tasked for carbon dioxide capture. *ACS Sust. Chem. Eng.* **2014**, *2* (9), 2117−2123.
(21) Smith, E. L.; Abbott, A. P.; Ryder, K. S. Deep eutectic solvents (DESs) and their applications. *Chem. Rev.* **2014**, *114* (21), 11060−11082.
(22) Wazeer, I.; Hadj-Kali, M. K.; Al-Nashef, I. M. Utilization of Deep Eutectic Solvents to Reduce the Release of Hazardous Gases to the Atmosphere: A Critical Review. *Molecules* **2021**, *26* (1), 75.
(23) Ali, E.; Hadj-Kali, M. K.; Mulyono, S.; Alnashef, I. Analysis of operating conditions for CO2 capturing process using deep eutectic solvents. *Int. J. Green. Gas Control.* **2016**, *47*, 342−350.
(24) Isik, M.; Zulfiqar, S.; Edhaim, F.; Ruiperez, F.; Rothenberger, A.; Mecerreyes, D. Sustainable Poly(Ionic Liquids) for CO_2 Capture Based on Deep Eutectic Monomers. *ACS Sustainable Chem. Eng.* **2016**, *4* (12), 7200−7208.
(25) Yang, X.; Zou, Q.; Zhao, T.; Chen, P.; Liu, Z.; Liu, F.; Lin, Q. Deep eutectic solvents as efficient catalysts for fixation of CO_2 to cyclic carbonates at ambient temperature and pressure through synergetic catalysis. *ACS Sustainable Chem. Eng.* **2021**, *9* (31), 10437−10443.
(26) Song, Z.; Hu, X.; Wu, H.; Mei, M.; Linke, S.; Zhou, T.; Qi, Z.; Sundmacher, K. Systematic screening of deep eutectic solvents as sustainable separation media exemplified by the CO_2 capture process. *ACS Sustainable Chem. Eng.* **2020**, *8* (23), 8741−8751.
(27) Abbott, A. P.; Harris, R. C.; Ryder, K. S.; D'Agostino, C.; Gladden, L. F.; Mantle, M. D. Glycerol eutectics as sustainable solvent systems. *Green Chem.* **2011**, *13* (1), 82−90.
(28) Zhang, Q.; De Oliveira Vigier, K.; Royer, S.; Jérôme, F. Deep eutectic solvents: syntheses, properties and applications. *Chem. Soc. Rev.* **2012**, *41* (21), 7108−7146.
(29) Zhang, Y.; Ji, X.; Lu, X. Choline-based deep eutectic solvents for CO_2 separation: Review and thermodynamic analysis. *Renewable Sustainable Energy Rev.* **2018**, *97*, 436−455.
(30) Trivedi, T. J.; Lee, J. H.; Lee, H. J.; Jeong, Y. K.; Choi, J. W. Deep eutectic solvents as attractive media for CO_2 capture. *Green Chem.* **2016**, *18* (9), 2834−2842.
(31) Leron, R. B.; Li, M.-H. Solubility of carbon dioxide in a choline chloride−ethylene glycol based deep eutectic solvent. *Thermochimica acta* **2013**, *551*, 14−19.
(32) Sarmad, S.; Xie, Y.; Mikkola, J.-P.; Ji, X. Screening of deep eutectic solvents (DESs) as green CO_2 sorbents: from solubility to viscosity. *New J. Chem.* **2017**, *41* (1), 290−301.
(33) Nasri, S.; Ajili, Y.; Jaidane, N.-E.; Kalugina, Y. N.; Halvick, P.; Stoecklin, T.; Hochlaf, M. Potential energy surface of the CO_2−N_2 van der Waals complex. *J. Chem. Phys.* **2015**, *142* (17), 174301.
(34) Plaza, M. G.; Pevida, C.; Arenillas, A.; Rubiera, F.; Pis, J. J. CO_2 capture by adsorption with nitrogen enriched carbons. *Fuel* **2007**, *86* (14), 2204−2212.
(35) Wang, S.-G.; Liao, X.-Y.; Cao, D.-B.; Huo, C.-F.; Li, Y.-W.; Wang, J.; Jiao, H. Factors controlling the interaction of CO_2 with transition metal surfaces. *J. Phys. Chem. C* **2007**, *111* (45), 16934−16940.
(36) Park, S.; Bae, H.; Ahn, J.; Lee, H.; Kwon, Y. Control of CO_2 Capture process on transition-metal-porphyrin-like graphene with mechanical strain. *ACS Omega* **2018**, *3* (9), 10554−10563.

(37) Schilter, D. Nickel doesn't get a slice of the pi. *Nat. Rev. Chem.* **2021**, *5* (7), 446−446.
(38) Dashtestani, F.; Nusheh, M.; Siriwongrungson, V.; Hongrapipat, J.; Materic, V.; Pang, S. CO_2 capture from biomass gasification producer gas using a novel calcium and iron-based sorbent through carbonation−calcination looping. *Ind. Eng. Chem. Res.* **2020**, *59* (41), 18447−18459.
(39) Megha; Mondal, K.; Ghanty, T. K.; Banerjee, A. Adsorption and activation of CO_2 on small-sized Cu−Zr bimetallic clusters. *J. Phys. Chem. A* **2021**, *125* (12), 2558−2572.
(40) Liu, X.; Sun, L.; Deng, W.-Q. Theoretical investigation of CO_2 adsorption and dissociation on low index surfaces of transition metals. *J. Phys. Chem. C* **2018**, *122* (15), 8306−8314.
(41) Wang, S.-G.; Cao, D.-B.; Li, Y.-W.; Wang, J.; Jiao, H. Chemisorption of CO_2 on nickel surfaces. *J. Phys. Chem. B* **2005**, *109* (40), 18956−18963.
(42) Vogel, W. M.; Smith, S. W. An electrochemical method for the determination of the solubility of a reactive gas in an electrolyte. *J. Electroanal. Chem. and Interface Electrochem.* **1968**, *18* (3), 215−218.
(43) Jiang, B.; Ma, J.; Yang, N.; Huang, Z.; Zhang, N.; Tantai, X.; Sun, Y.; Zhang, L. Superbase/acylamido-based deep eutectic solvents for multiple-site efficient CO_2 absorption. *Energy Fuels* **2019**, *33* (8), 7569−7577.
(44) Flowers, B. S.; Mittenthal, M. S.; Jenkins, A. H.; Wallace, D. A.; Whitley, J. W.; Dennis, G. P.; Wang, M.; Turner, C. H.; Emel'yanenko, V. N.; Verevkin, S. P.; Bara, J. E. 1,2,3-Trimethoxypropane: A glycerol-derived physical solvent for CO_2 absorption. *ACS Sust. Chem. Eng.* **2017**, *5* (1), 911−921.
(45) Hornig, M.; Klamt, A. COSMOfrag: A novel tool for high-throughput adme property prediction and similarity screening based on quantum chemistry. *J. Chem. Inf. Model.* **2005**, *45* (5), 1169−1177.
(46) Ali, E.; Hadj-Kali, M. K.; Alnashef, I. Modeling of CO_2 Solubility in Selected Imidazolium-Based Ionic Liquids. *Chem. Eng. Commun.* **2017**, *204* (2), 205−215.
(47) Steffen, C.; Thomas, K.; Huniar, U.; Hellweg, A.; Rubner, O.; Schroer, A. TmoleX-a graphical user interface for TURBOMOLE. *J. Comput. Chem.* **2010**, *31* (16), 2967−2970.
(48) Perdew, J. P. Density-functional approximation for the correlation energy of the inhomogeneous electron gas. *Phys. Rev. B* **1986**, *33* (12), 8822.
(49) Schäfer, A.; Huber, C.; Ahlrichs, R. Fully optimized contracted gaussian basis sets of triple zeta valence quality for atoms Li to Kr. *J. Chem. Phys.* **1994**, *100* (8), 5829−5835.
(50) Ghaedi, H.; Ayoub, M.; Sufian, S.; Hailegiorgis, S. M.; Murshid, G.; Khan, S. N. Thermal stability analysis, experimental conductivity and pH of phosphonium-based deep eutectic solvents and their prediction by a new empirical equation. *J. Chem. Thermodyn.* **2018**, *116*, 50−60.
(51) Florindo, C.; Oliveira, F. S.; Rebelo, L. P. N.; Fernandes, A. M.; Marrucho, I. M. Insights into the synthesis and properties of deep eutectic solvents based on cholinium chloride and carboxylic acids. *ACS Sust. Chem. Eng.* **2014**, *2* (10), 2416−2425.
(52) Hartman, M.; Trnka, O.; Šolcová, O. Thermal decomposition of aluminum chloride hexahydrate. *Ind. Eng. Chem. Res.* **2005**, *44* (17), 6591−6598.
(53) Wang, Y.; Zhang, H.; Zhu, Y.; Dai, Z.; Bao, H.; Wei, Y.; Cai, W. Au-NP-decorated crystalline feocl nanosheet: Facile synthesis by laser ablation in liquid and its exclusive gas sensing response to HCl at room temperature. *Adv. Mater. Interfaces* **2016**, *3* (9), 1500801.
(54) Neubauer, S. S.; Krause, R. K.; Schmid, B.; Guldi, D. M.; Schmid, G. Overpotentials and faraday efficiencies in CO_2 electrocatalysis−the Impact of 1-ethyl-3-methylimidazolium trifluoromethanesulfonate. *Adv. Energy Mater.* **2016**, *6* (9), 1502231.
(55) Zhang, L.; Wu, N.; Zhang, J.; Hu, Y.; Wang, Z.; Zhuang, L.; Jin, X. Imidazolium ions with an alcohol substituent for enhanced electrocatalytic reduction of CO_2. *ChemSusChem* **2017**, *10* (24), 4824−4828.
(56) Levi, M. D.; Demadrille, R.; Pron, A.; Vorotyntsev, M. A.; Gofer, Y.; Aurbach, D. Application of a novel refinement method for accurate determination of chemical diffusion coefficients in electroactive materials by potential step technique. *J. Electrochem. Soc.* **2005**, *152* (2), E61.
(57) García Rey, N.; Dlott, D. D. Structural transition in an ionic liquid controls CO_2 Electrochemical Reduction. *J. Phys. Chem.* **2015**, *119* (36), 20892−20899.
(58) Klamt, A.; Eckert, F.; Arlt, W. COSMO-RS: An alternative to simulation for calculating thermodynamic properties of liquid mixtures. *Annu. Rev. Chem. Biomol. Eng.* **2010**, *1*, 101−122.
(59) Eckert, F.; Klamt, A. *COSMOtherm*, Version C2, 2013; Vol. *1*.
(60) Gutsev, G. L.; Bartlett, R. J.; Compton, R. N. Electron affinities of CO_2, OCS, and CS_2. *J. Chem. Phys.* **1998**, *108* (16), 6756−6762.
(61) Mascetti, J. Carbon dioxide coordination chemistry and reactivity of coordinated CO_2. In *Carbon Dioxide as Chemical Feedstock*; Wiley Online Library: Germany, 2010; pp 55−88.
(62) Scherer, W.; Eickerling, G.; Shorokhov, D.; Gullo, E.; McGrady, G. S.; Sirsch, P. Valence shell charge concentrations and the Dewar−Chatt−Duncanson bonding model. *New J. Chem.* **2006**, *30* (3), 309−312.

https://doi.org/10.1021/acsomega.2c00672
ACS Omega 2022, 7, 14102−14112